RESEARCH ARTICLE

small methods
www.small-methods.com

Controllable Synthesis of Carbon Yolk-Shell Microsphere and Application of Metal Compound–Carbon Yolk-Shell as Effective Anode Material for Alkali-Ion Batteries

Yeong Beom Kim, Hyo Yeong Seo, Sang-Hyun Kim, Tae Ha Kim, Jae Hyeon Choi, Jung Sang Cho, Yun Chan Kang,* and Gi Dae Park**

Recently, nanostructured carbon materials, such as hollow-, yolk-, and core-shell-configuration, have attracted attention in various fields owing to their unique physical and chemical properties. Among them, yolk-shell structured carbon is considered as a noteworthy material for energy storage due to its fast electron transfer, structural robustness, and plentiful active reaction sites. However, the difficulty of the synthesis for controllable carbon yolk-shell has been raised as a limitation. In this study, novel synthesis strategy of nanostructured carbon yolk-shell microspheres that enable to control morphology and size of the yolk part is proposed for the first time. To apply in the appropriate field, cobalt compounds-carbon yolk-shell composites are applied as the anode of alkali-ion batteries and exhibit superior electrochemical performances to those of core-shell structures owing to their unique structural merits. Co_3O_4-C hollow yolk-shell as a lithium-ion battery anode exhibits a long cycling lifetime (619 mA h g^{-1} for 400 cycles at 2 A g^{-1}) and excellent rate capability (286 mA h g^{-1} at 10 A g^{-1}). The discharge capacities of $CoSe_2$-C hollow yolk-shell as sodium- and potassium-ion battery anodes at the 200th cycle are 311 mA h g^{-1} at 0.5 A g^{-1} and 268 mA h g^{-1} at 0.2 A g^{-1}, respectively.

1. Introduction

Nanostructured carbon materials, such as hollow-, yolk-, and core-shell structures have been intensively investigated over the past decade.[1–4] In various application fields, including energy storage and conversion, catalysis, fuel cell, supercapacitors, water, and air purification, and separation, nanostructured carbon materials have been efficiently utilized considering their large surface area, pore volume, high structural and mechanical stabilities, and good electrical conductivity.[5–10] Owing to the structural differences (hollow-, yolk-, and core-shell (do not contain void)), they could be appropriately used in required applications.

Synthesis strategies for realizing nanostructured carbon materials have been representatively proposed by the surfactant-directing co-assembly method. Wang et al. synthesized hierarchically porous carbon spheres with a yolk-shell structure using a new gradient sol–gel process combined with a surfactant-directed co-assembly for high-performance supercapacitors.[11] Particularly, the sizes of the yolk and shell were controlled by simply adjusting the amount of the cationic surfactant cetyltrimethylammonium bromide or tetraethoxysilane (TEOS). They found that yolk-shell carbon with hierarchical pore architectures exhibited a high performance with a high specific capacitance and good rate capabilities. Zhang et al. reported porous yolk-shell carbon sphere materials prepared via the extended Stober method.[12] Their morphologies, including the pore volume, specific surface area, and yolk ratio, could be well adjusted by controlling the TEOS concentration. These samples had different porosities and yolk ratios, which influenced the electrolyte wetting, K^+ diffusion distance, and reversible adsorption of K^+ in K-ion batteries (KIBs).

Recently, highly porous yolk-shell carbon materials with nanostructures were utilized as reservoirs for ultrafine nanocrystals.[13–18] Hierarchical micro- and mesoporous carbon materials could infiltrate ultrasmall chalcogen (sulfur or selenium) components and be applied to cathode materials for lithium-chalcogen batteries. Chen et al. synthesized multishelled hollow carbon nanosphere-encapsulated sulfur composites with a high sulfur loading (86 wt%) using aqueous emulsions and in situ sulfur impregnation.[19] In addition, metal compound nanocrystals could be embedded into yolk-shell carbon materials during the carbonization process using metal-organic frameworks (MOFs). Wang et al. introduced a strategy

Y. B. Kim, H. Y. Seo, S.-H. Kim, T. H. Kim, J. H. Choi, G. D. Park
Department of Advanced Materials Engineering
Chungbuk National University
Chungdae-ro 1, Seowon-gu, Cheongju, Chungbuk 28644, Republic of Korea
E-mail: gdpark@chungbuk.ac.kr

J. S. Cho
Department of Engineering Chemistry
Chungbuk National University
Chungdae-ro 1, Seowon-gu, Cheongju, Chungbuk 28644, Republic of Korea
E-mail: jscho@cbnu.ac.kr

Y. C. Kang
Department of Materials Science and Engineering
Korea University
Anam-dong, Seongbuk-gu, Seoul 136–713, Republic of Korea
E-mail: yckang@korea.ac.kr

The ORCID identification number(s) for the author(s) of this article can be found under https://doi.org/10.1002/smtd.202201370.

DOI: 10.1002/smtd.202201370

of synthesizing yolk-shell N-doped porous carbon embedded with CoO nanoparticles.[20] By controlling atmosphere for pyrolysis, in situ formation of carbon yolk-shell configuration and ultrafine CoO nanocrystals composite were facilitated. However, despite the various applications of nanostructured carbon materials, preparation methods that can freely control the yolk size for nanostructured carbon materials have rarely been reported.

In this study, strategies for synthesis of hollow yolk-shell and dense core-shell-structured carbon microspheres and control of the carbon yolk size in the carbon microsphere are introduced. In our previous research, the yolk-shell-structured carbon microsphere was prepared using spray pyrolysis and the removal process was tin selenide evaporation.[21] The prepared yolk-shell carbon microsphere was applied as a cathode material for lithium–sulfur batteries. For further synthesis development, the change in the yolk size according to the ratio of polyvinylpyrrolidone (PVP) and sucrose was observed. From a hollow yolk-shell structure to a dense core-shell structure with almost no empty space as a yolk gradually forms, to the best of our knowledge, a method to easily control the carbon nanostructure is proposed for the first time. In addition, magnesium oxide was added to improve the pore volume capable of impregnating a metal salt. Cobalt compounds (cobalt oxide and cobalt selenide) were selected as the first target materials to form nanostructured cobalt compound–carbon composites as anode materials for alkali-ion batteries.

2. Results and Discussion

The novel rational formation mechanism of the yolk-shell-structured carbon microsphere, wherein the yolk size could be controlled, is illustrated in **Scheme 1**. The spray pyrolysis process facilitated the formation of a uniform nanocomposite at the nanoscale, which was attributed to the formation from a droplet containing solvated metal ions. As shown in Scheme 1a, a SnO_2-MgO-C@C microsphere was prepared from a spray solution, which contained tin oxalate, magnesium nitrate, and PVP. Owing to the phase segregation effect, PVP migrated to the outside of the microsphere, and the incompletely migrated PVP remained in the core part with SnO_2 and MgO nanocrystals. The partially phase-segregated SnO_2-MgO-C@C microsphere was transformed into SnSe-MgSe-C@C by selenization. Subsequently, an immediate tin selenide component was evaporated under a high temperature of 1000 °C. The obtained MgSe-C@C microsphere was etched by an HCl/HNO_3 solution, which resulted in the formation of a hollow-yolk C@void@C microsphere. Scheme 1b shows that the formation of a dense yolk carbon was enabled according to the addition of

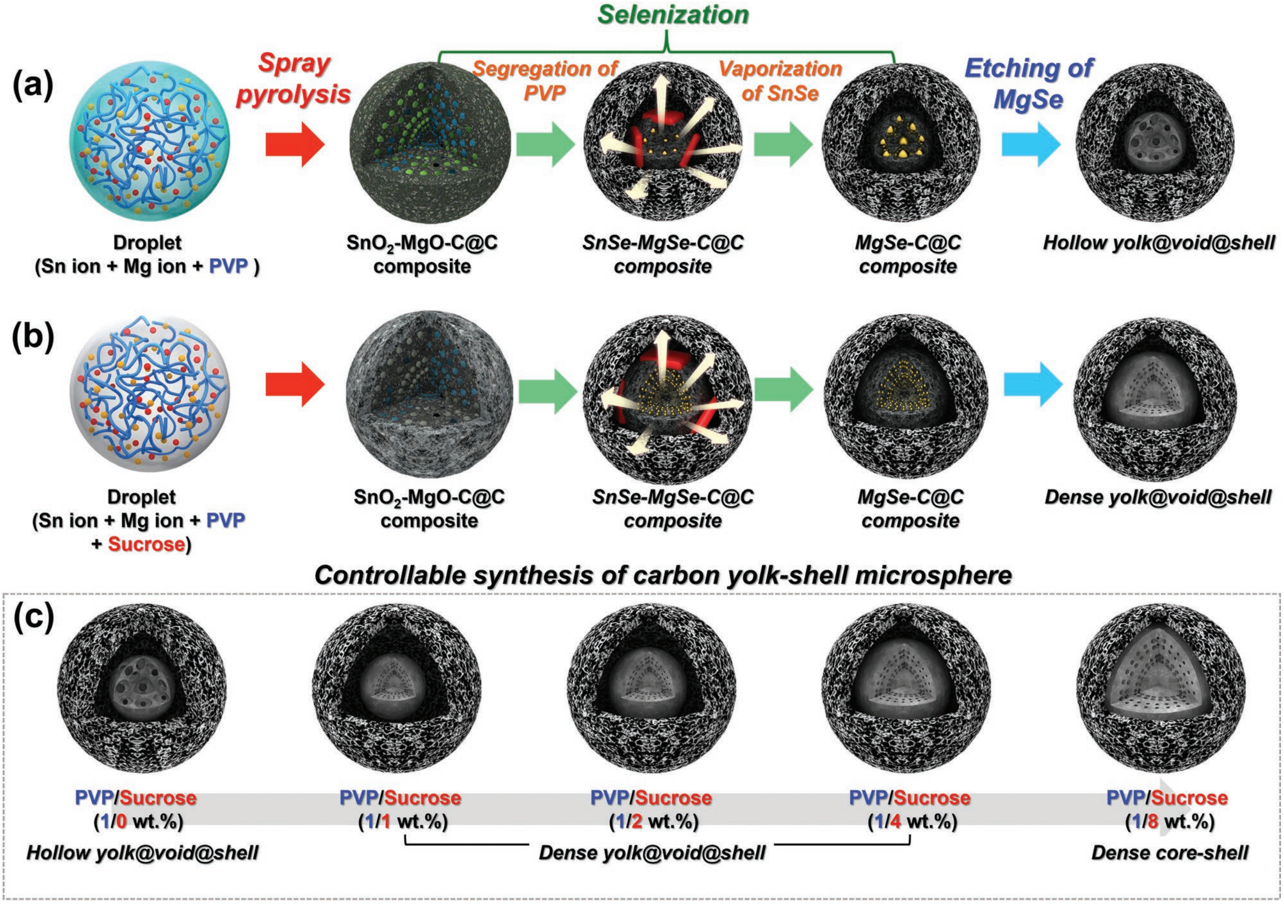

Scheme 1. Illustration of the formation mechanism for a) hollow yolk@void@shell carbon microsphere, b) dense yolk@void@shell carbon microsphere, and c) the change in yolk size as the ratio of PVP/sucrose.

sucrose in the PVP-based solution. In spray pyrolysis using the same spray solution with added sucrose in the PVP-based solution, the partial phase segregation occurred similarly. However, in this process, sucrose was easily decomposed to an amorphous carbon owing to its lower decomposition temperature (185 °C) than that of PVP (380 °C). Therefore, an SnO_2-MgO and carbon (derived from sucrose) composite and carbon shell (derived from the migrated PVP) were formed in the yolk and shell parts, respectively. In this synthesis process, the change in yolk size could be expected with the ratio of PVP and sucrose, as described in Scheme 1c. When the ratio of sucrose was continuously increased, carbon microspheres with a core-shell structure without voids were formed.

The morphological characteristics of the spray-pyrolyzed precursor, posttreated powder, wherein the tin component was eliminated by evaporation of tin selenide, and etched carbon microsphere were compared by scanning electron microscopy (SEM) images, as shown in **Figures 1** and Figure S1–S3, Supporting Information. The spray-pyrolyzed precursor in Figure S1a–e, Supporting Information shows a similar spherical microsphere. As the spray-pyrolyzed precursor was formed by consecutive drying and decomposition process from a droplet containing solvated metal ions, the formation of a uniform metal compound–carbon nanocomposite was facilitated. However, the magnified SEM images in Figures 1a–e show a slight difference according to the increase in the ratio of sucrose in PVP/sucrose. Owing to the phase segregation effect during the spray pyrolysis process, PVP migrated to the outside of the microsphere, and the incompletely migrated PVP and sucrose remained in the core part with SnO_2 and MgO nanocrystals. After posttreatment via selenization and evaporation of tin selenide at 1000 °C, dense structured microspheres were transformed into various yolk-shell-structured microspheres, as shown in Figures 1f–j. In the case of the absence of sucrose in the spray solution, a hollow yolk@void@C microsphere was observed, as shown in Figure 1f. As ratio of sucrose in the spray solution was gradually increased, the dense structured yolk grew. The void formation was attributed to evaporation of the tin selenide component, which was formed during selenization. In the low-resolution SEM images in Figure S2a–e, Supporting Information, some of the crystals in the microsphere were observed, confirmed as MgSe component according to the X-ray diffraction (XRD) data in Figure S4, Supporting Information. MgSe crystals were completely eliminated by etching under an HCl/HNO_3 solution. The pure carbon microspheres with various nanostructures are presented in Figure 1k–o. The low-resolution SEM images and XRD data in Figure S3a–e and Figure S4, Supporting Information, respectively, confirm the removal of the MgSe component. To demonstrate the presence of immediate tin selenide component, the XRD analysis of powders, which were posttreated at 700 °C from spray-pyrolyzed precursors, was conducted as shown in Figure S5, Supporting Information. SnSe phase was confirmed in all samples regardless of the ratio of PVP/sucrose. The peaks related to

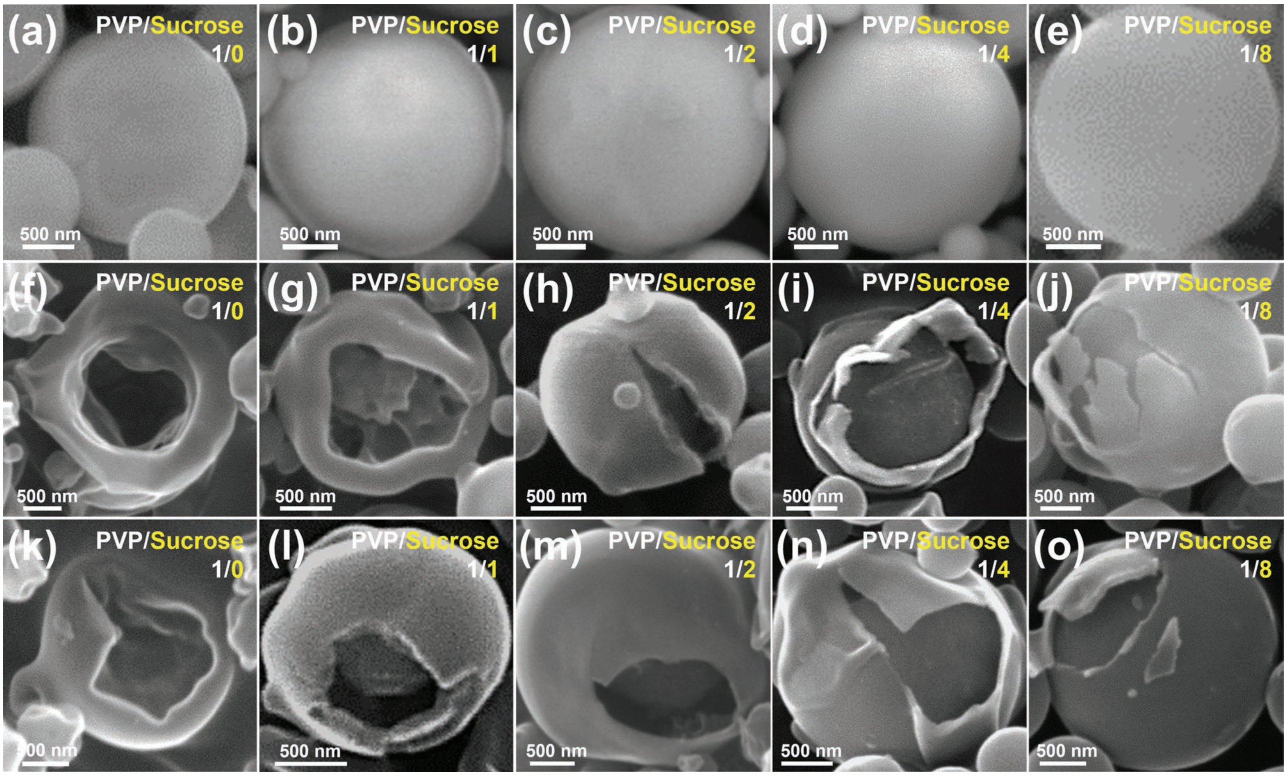

Figure 1. Morphological characteristics of a–e) SEM images of SnO_2-MgO-C@C composite precursors prepared from the spray solution containing Sn oxalate, sucrose, Mg nitrate, and PVP with different ratio of PVP/sucrose, f–j) SEM images of MgSe-C@C obtained after selenization of precursor, and k–o) SEM images of carbon yolk-shell after etching process: a,f,k) PVP/Sucrose 1/0 wt.%, b,g,l) PVP/Sucrose 1/1 wt%, c,h,m) PVP/Sucrose 1/2 wt%, d,i,n) PVP/Sucrose 1/4 wt%, and e,j,o) PVP/Sucrose 1/8 wt%.

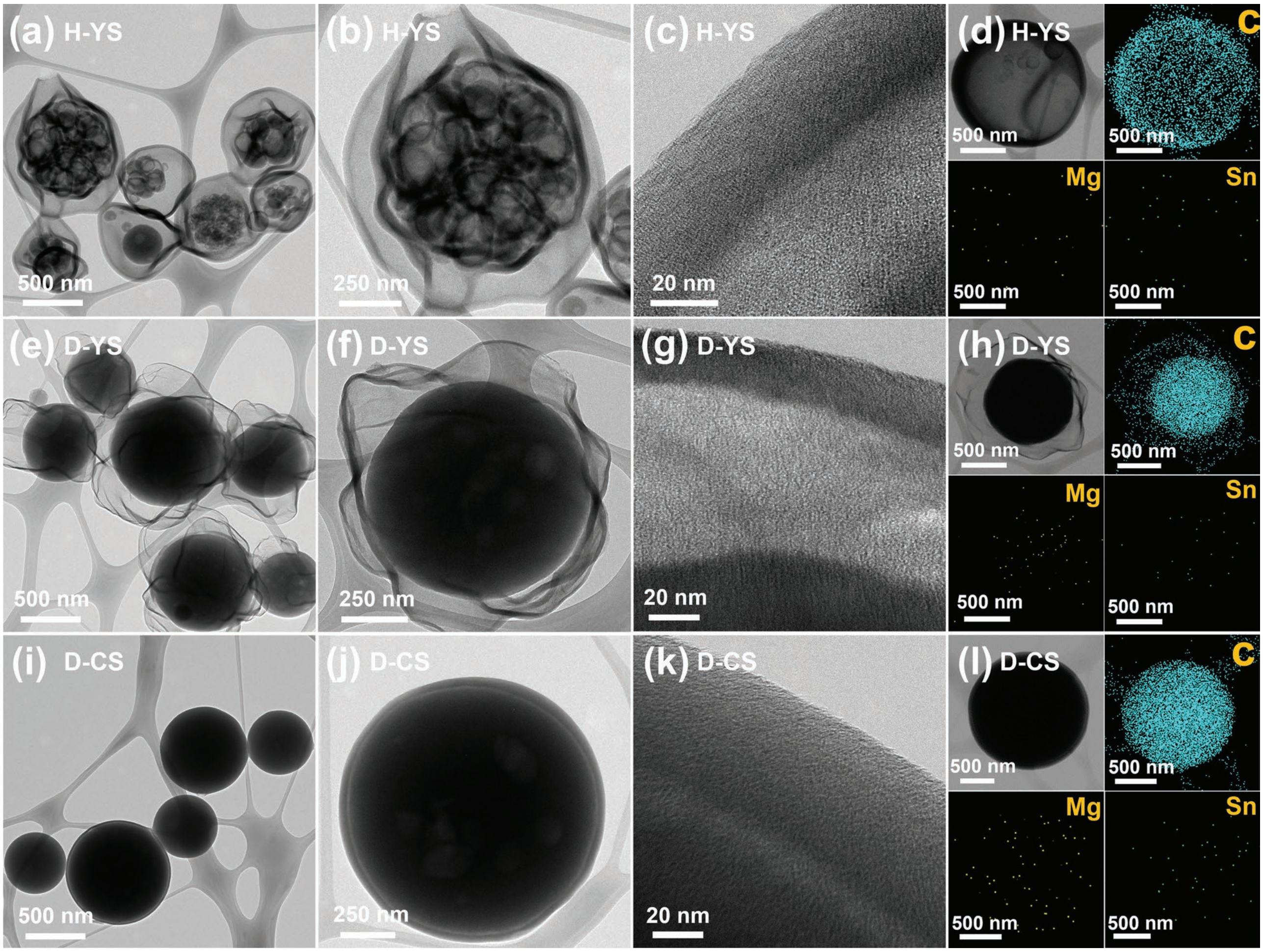

Figure 2. TEM images and elemental mapping images a–d) H-YS, e–h) D-YS, and i–l) D-CS microspheres: a,b,e,f,i,j) TEM images, c,g,k) HR-TEM images, and d,h,l) elemental mapping images.

MgSe were not observed in the XRD patterns in Figure S5a, Supporting Information, indicating that the MgSe was formed near 1000 °C as confirmed by XRD data in Figure S4, Supporting Information.

The specific morphological characteristic of the carbon yolk-shell microsphere according to the ratio of PVP/sucrose was compared by transmission electron microscopy (TEM), as shown in **Figure 2**. The carbon yolk-shell microspheres prepared from spray solutions with a ratio of PVP/sucrose (1/0, 1/4, 1/8 wt%) are denoted as H-YS, D-YS, and D-CS (hollow yolk@void@shell, dense yolk@void@shell, and dense core-shell, respectively). As confirmed by the SEM image in Figure 1k, the low-resolution TEM images in Figure 2a,b, Supporting Information reveal the formation of hollow nanocarbon aggregate@void@shell configuration (H-YS). The partial phase segregation of PVP as well as carbonization of PVP around MgSe crystals facilitated the formation of the hollow nanocarbon aggregate. The high-resolution TEM (HR-TEM) image in Figure 2c reveals a mesoporous carbon shell, which was derived from the carbonization of PVP and removal of MgSe nanocrystals. The elemental maps in Figure 2d, show a pure carbon component and complete elimination of Sn and Mg components. As a ratio of sucrose in the PVP-containing spray solution was increased, the figuration of the yolk part was filled with carbon component, as confirmed by Figure 2e,f. During the spray pyrolysis, the carbon component, which was derived from the decomposition of sucrose, was not migrated to the shell but formed a dense composite with Sn, Mg, and C. Owing to this difference in behavior between PVP and sucrose, a controllable synthesis of a carbon yolk-shell microsphere was possible. As MgSe nanocrystals embedded into the dense carbon yolk were eliminated by the acid treatment, a partially porous yolk structure was formed in D-YS, as shown in Figure 2f. The HR-TEM image in Figure 2g shows micro- and mesoporous structures of the yolk and shell of D-YS. The elemental maps reveal the formation of a pure dense carbon yolk-shell microsphere. The TEM images in Figure 2i,j show the formation of a carbon core-shell with a small void (D-CS). As the ratio of sucrose in the spray solution was sufficiently high, the carbon component, which was derived from sucrose, was thoroughly filled with voids in the microsphere. The HR-TEM image in Figure 2k shows the small void between the core and shell and mesopores. The elemental maps in Figure 2l show the formation of a pure dense core-shell carbon microsphere.

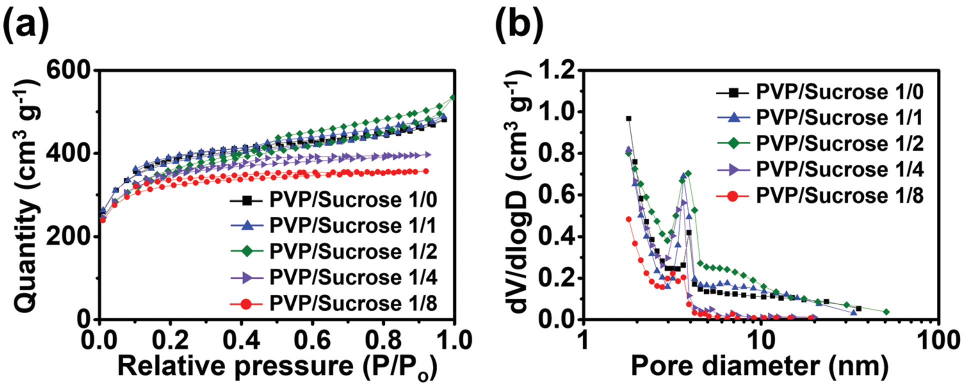

Figure 3. a) N_2 gas adsorption and desorption isotherm and b) BJH pore-size distribution of carbon yolk-shell microspheres with different ratio of PVP/sucrose.

The specific surface areas and pore structures of various carbon yolk-shell microspheres were analyzed by Brunauer–Emmett–Teller (BET) and Barrett–Joyner–Halenda (BJH) measurements. In the N_2 adsorption–desorption isotherms shown in **Figure 3**a, combinations of type-I and IV isotherms were observed for the carbon yolk-shell microspheres, which indicate hierarchical porous structures. The BET surface areas of the carbon yolk-shell microspheres prepared from spray solutions with ratio of PVP/sucrose (1/0, 1/1, 1/2, 1/4, 1/8 wt%), were 1218, 1171, 1154, 1113, and 1018 m^2 g^{-1}, whereas their pore volumes were 0.74, 0.71, 0.69, 0.61, and 0.55 cm^3 g^{-1}, respectively. The specific surface areas and pore volumes of the carbon yolk-shell microspheres tended to gradually decrease as a ratio of sucrose in the PVP-containing spray solution was increased. Thus, the PVP-derived carbon had a larger pore volume than that of the sucrose-derived carbon when it was carbonized under the conditions of this study. This was additionally demonstrated by the pore size distribution analysis of the carbon yolk-shell microspheres, as shown in Figure 3b. As a ratio of sucrose was increased, the micropores formed from PVP gradually decreased, which contributed to the reduction in the specific surface area. Compared with the results of previous studies, the specific surface area was almost doubled owing to the magnesium selenide removal effect according to the addition of the magnesium salt in the spray solution.[21]

The highly porous and well-designed carbon could be utilized as a reservoir for ultrafine nanocrystals. **Scheme 2**

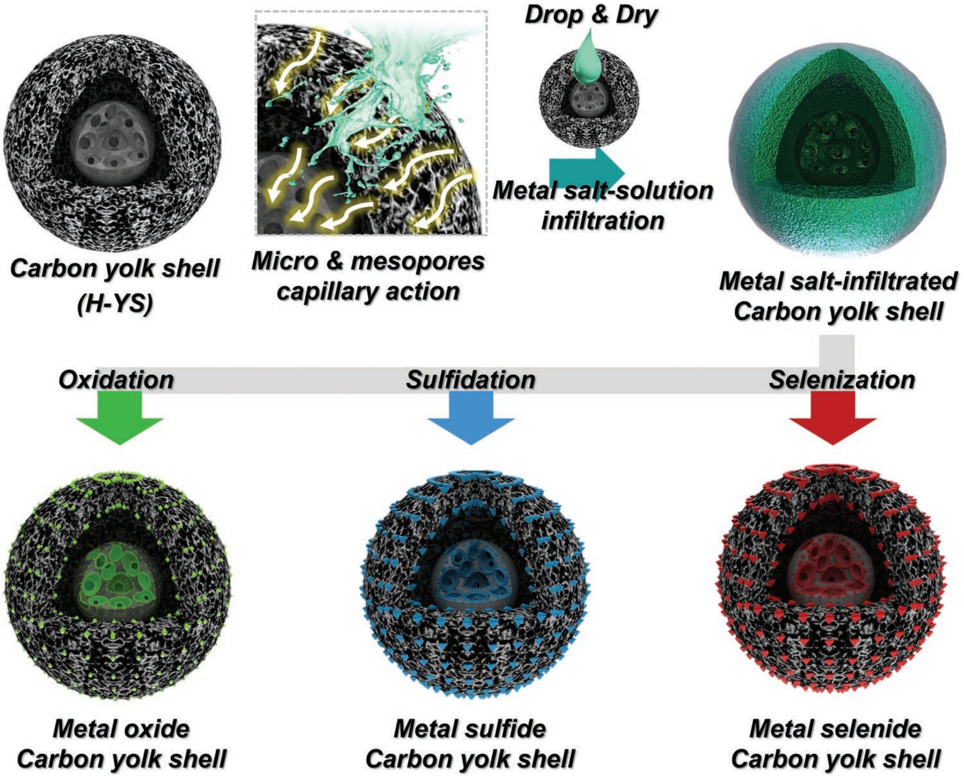

Scheme 2. Formation mechanism of the metal compounds embedded in porous hollow carbon yolk-shell microspheres.

illustrates the strategies for the synthesis of metal compounds uniformly embedded in porous hollow carbon yolk-shell microspheres. The prepared carbon yolk-shell microsphere acted as a matrix with a large pore volume, which enabled the infiltration of metal salt solutions. The metal salt uniformly impregnated in the small pores of both yolk and shell owing to capillary action could form various phases depending on the heat treatment conditions. The oxidation, sulfidation, and selenization processes transformed metal salt-C into metal oxide-C, metal sulfide-C, and metal selenide-C, respectively. This shows the characteristics of the novel synthesis method with free control over composition as well as various shapes.

The cobalt compounds-carbon composite yolk-shell was applied as a target material. The carbon yolk-shell consisting of ultrafine cobalt oxide nanocrystals was prepared via a simple oxidation process under the atmosphere. The morphological characteristics of cobalt oxide-C hollow yolk-shell (denoted as Co_3O_4-H-YS) and dense core-shell (denoted as Co_3O_4-D-CS) prepared by the spray solution with ratios of PVP/sucrose 1/0 and 1/8 wt.%, respectively, are shown in **Figure 4**. The TEM images in Figure 4a,b confirm that cobalt oxide nanocrystals were uniformly impregnated into the microsphere through darken the brightness of the hollow nanocarbon aggregate and shell. Moreover, the hollow nanosphere aggregate@void@shell configurations were well maintained even through the oxidation process. The HR-TEM image in Figure 4c reveals that the ultrafine cobalt oxide nanocrystals (smaller than 5 nm) were embedded in the carbon matrix. The clear lattice fringes separated by 0.24 and 0.28 nm corresponded to the (311) and (220) crystal planes of the Co_3O_4 phase, respectively. The SAED pattern in Figure 4d also confirms the Co_3O_4 phase. The corresponding elemental maps in Figure 4e verified the presence of C, Co, and O elements, homogeneously distributed in H-YS. The morphological characteristics of the cobalt oxide nanocrystals

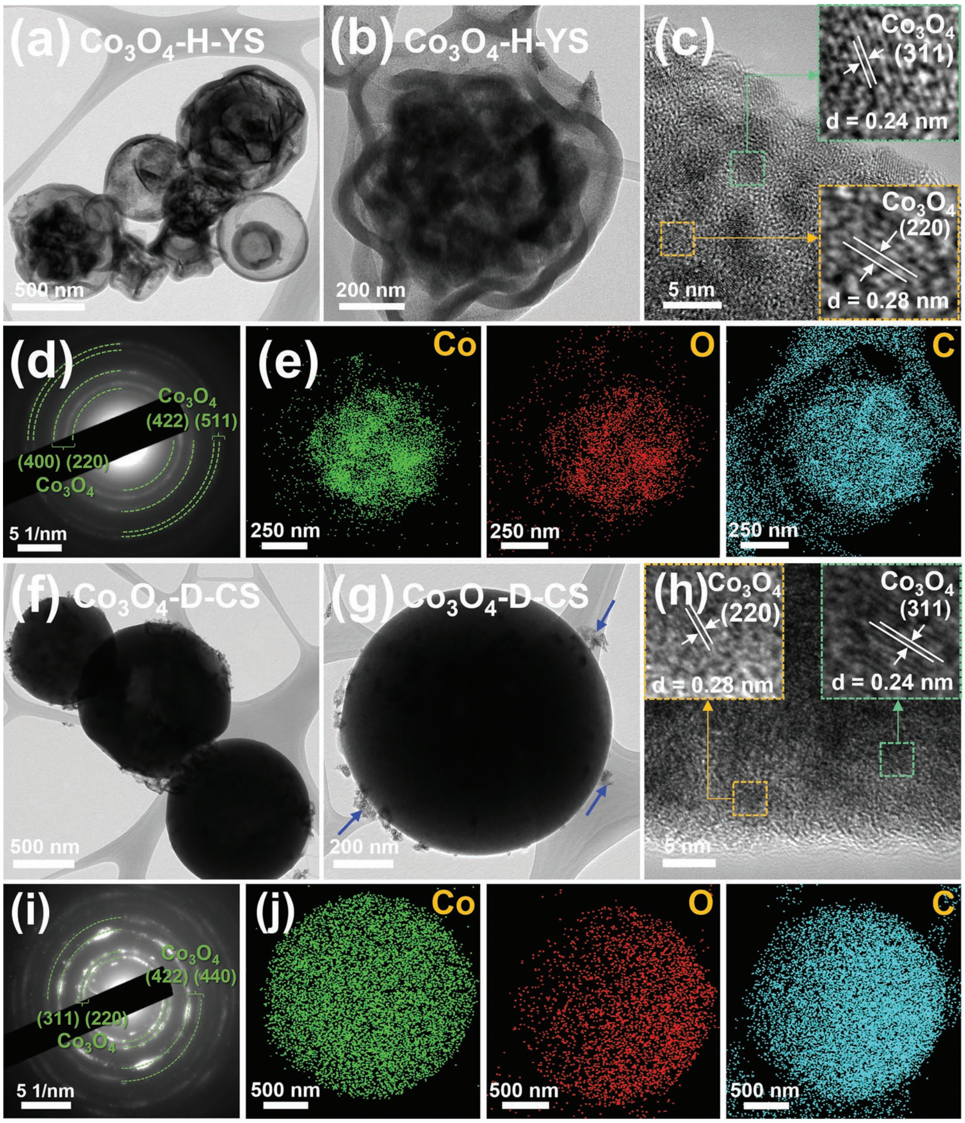

Figure 4. TEM images, SAED patterns, and elemental mapping images of a–e) Co_3O_4-H-YS and f–j) Co_3O_4-D-CS microspheres: a,b,f,g) TEM images, c,h) HR-TEM images, d,i) SAED patterns, and e,j) elemental mapping images.

embedded in D-CS (Co_3O_4-D-CS) are shown in Figures 4f–j. The TEM images in Figure 4f,g reveal that the cobalt salt infiltration solution was deeply and uniformly impregnated in the dense yolk carbon and shell. Some nanocrystals were not completely infiltrated in the yolk carbon, as indicated by arrows in Figure 4g. The HR-TEM images show clear lattice fringes separated by 0.24 and 0.28 nm, corresponding to the (311) and (220) crystal planes of the Co_3O_4 phase, respectively. The SAED pattern in Figure 4i also confirms the Co_3O_4 phase. The elemental maps in Figure 4j indicate the formation of a dense structured Co_3O_4-C microsphere.

To demonstrate the possibility of synthesis of various metal compounds, the cobalt-salt-infiltrated carbon yolk-shell was transformed into a cobalt selenide-carbon yolk-shell by a simple selenization process. The morphological properties of cobalt selenide hollow yolk-shell (denoted as $CoSe_2$-H-YS) and dense core-shell (denoted as $CoSe_2$-D-CS) prepared by the spray solution with ratios of PVP/sucrose 1/0 and 1/8 wt.%, respectively are presented in **Figure 5**. Compared with the TEM images of Co_3O_4-H-YS and Co_3O_4-D-CS in Figure 4, the overall characteristics were similar; however, a slight difference in the crystallinity of the nanocrystals was confirmed. Owing to the high reactivity of the H_2Se gas during the selenization process, relatively larger cobalt selenide nanocrystals were observed (Figure 5). Even though the selenization process, hollow nanosphere aggregate@void@shell configurations were well maintained, as shown in Figure 5a,b. Moreover, small cobalt selenide nanocrystals (smaller than 10 nm) were evenly decorated on the carbon matrix (Figure 5c). The HR-TEM images show clear lattice fringes separated by 0.26 and 0.29 nm, corresponding to the (210) and (220) crystal planes of the $CoSe_2$ phase, respectively. The SAED pattern in Figure 5d also confirms the $CoSe_2$ phase. The elemental maps in Figure 5e indicate the presence of C, Co, and Se elements, homogeneously distributed in H-YS. The TEM

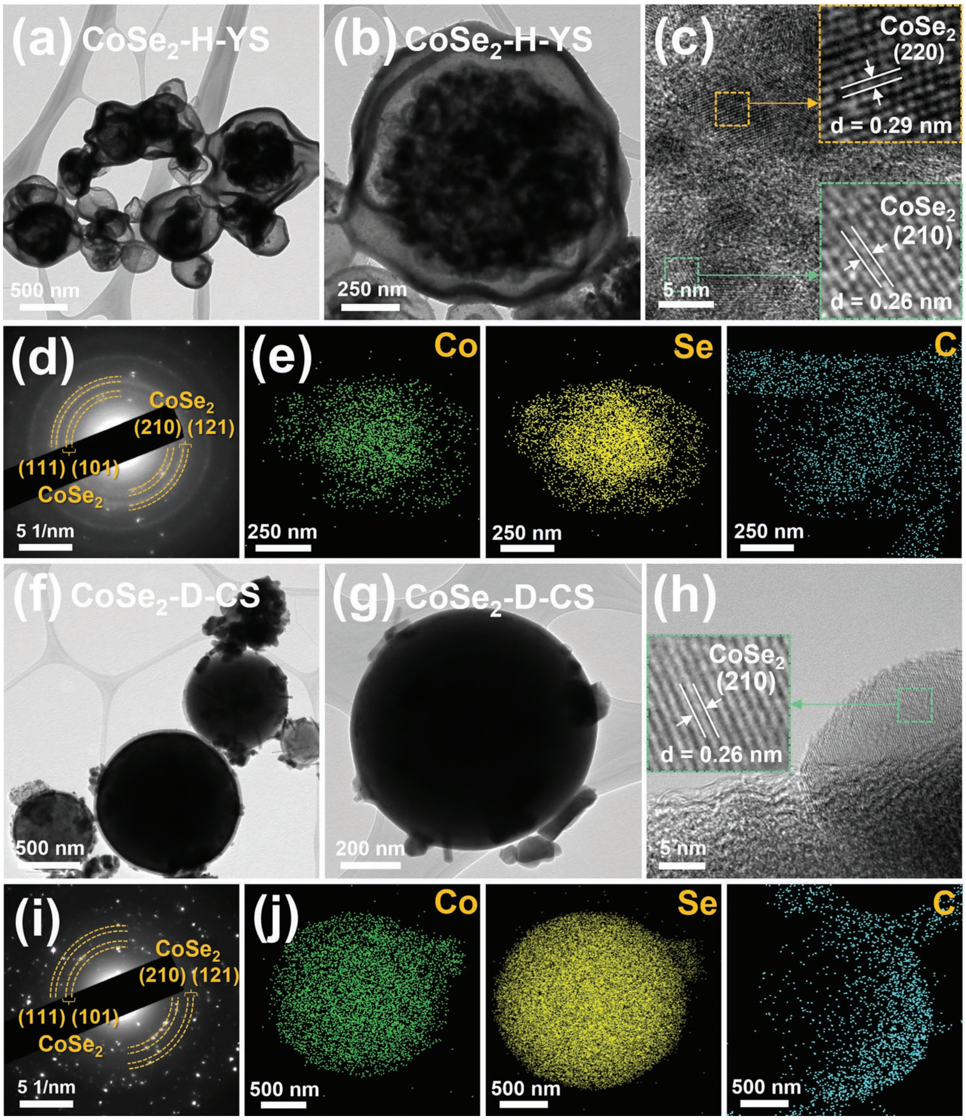

Figure 5. TEM images, SAED patterns, and elemental mapping images of a–e) $CoSe_2$-H-YS and f–j) $CoSe_2$-D-CS microspheres: a,b,f,g) TEM images, c,h) HR-TEM images, d,i) SAED patterns, and e,j) elemental mapping images.

images in Figure 5f,g indicate the formation of a dense cobalt selenide-C microsphere. Some large $CoSe_2$ crystals, formed by Ostwald ripening during the selenization process, were observed. The HR-TEM images show clear lattice fringes separated by 0.26 nm, corresponding to the (210) crystal planes of the $CoSe_2$ phase. The SAED pattern in Figure 5i also confirms the $CoSe_2$ phase. The elemental maps in Figure 5j indicate the formation of a dense $CoSe_2$-carbon yolk-shell microsphere.

The crystal structures and chemical states of the cobalt compound (Co_3O_4 and $CoSe_2$)–carbon yolk-shell samples were characterized by XRD and X-ray photoelectron spectroscopy (XPS) analysis, as shown in **Figure 6**a,b and Figures S6, and S7, Supporting Information, respectively. The XRD patterns in Figure 6a reveal the formation of Co_3O_4 phase in Co_3O_4-H-YS and confirm that $CoSe_2$ phase in $CoSe_2$-H-YS is composed of orthorhombic $CoSe_2$ and cubic $CoSe_2$ (denoted *o*-$CoSe_2$ and *c*-$CoSe_2$, respectively). The mean crystallite sizes of Co_3O_4 and $CoSe_2$ in Co_3O_4-H-YS and $CoSe_2$-H-YS, calculated by the widths of the (311) and (120) peaks using the Scherrer equation, were 8.6 and 25.4 nm, respectively. To elucidate the chemical states of the cobalt compounds (Co_3O_4 and $CoSe_2$)–carbon yolk-shell samples, they were analyzed by an XPS measurement. In the Co 2*p* spectra of Co_3O_4-H-YS and $CoSe_2$-H-YS in Figure 6b, different fitted peaks according to the binding energies of cobalt and anions (O or Se) were observed. The Co 2*p* spectra of Co_3O_4-H-YS contained Co $2p_{1/2}$ and Co $2p_{3/2}$ spin–orbit peaks (Co^{2+} at 796.3 and 781.3 eV and Co^{3+} at 794.5 and 779.5 eV) as well as four satellite peaks (indicated as Sat.),[22,23] whereas the spectra of Co 2*p* for $CoSe_2$-H-YS exhibited deconvoluted peaks corresponding to $CoSe_2$ (Co^{2+}) and cobalt selenite (Co^{2+}).[24,25]

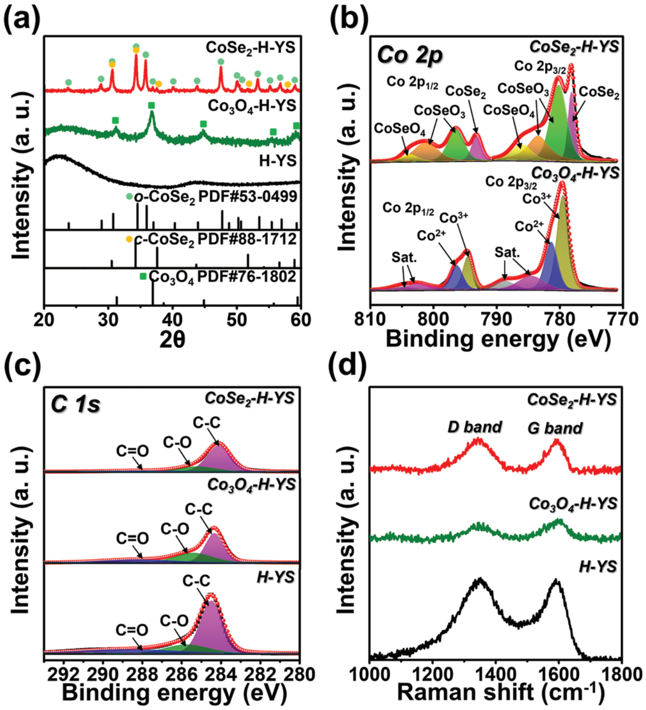

Figure 6. Crystal structures and chemical states of Co_3O_4-H-YS, $CoSe_2$-H-YS, and H-YS microspheres: a) XRD patterns, b–c) XPS spectra corresponding to b) Co 2p, c) C 1s, and d) Raman spectra.

Some of the cobalt selenite layers over $CoSe_2$-H-YS were formed through the partial surface oxidation of $CoSe_2$ nanocrystals in the atmosphere. The O 1*s* XPS spectrum of Co_3O_4-H-YS in Figure S6a, Supporting Information was decomposed into three peaks at 529.5, 530.9, and 532.7 eV, corresponding to lattice oxygen atoms (O1), oxygen vacancies (O2), and oxygen atoms in the physi/chemisorbed water (O3), respectively.[26,27] The Se 3*d* spectrum of $CoSe_2$-H-YS exhibited two distinct peaks at 54.3 and 55.1 eV corresponding to Se $3d_{5/2}$ and Se $3d_{3/2}$, respectively.[24,28] As confirmed in Figure 6b, the peaks at 58.3, 59.2, and 59.9 eV was related to the cobalt selenite layer.[24,28,29] To characterize the carbon components in the carbon yolk-shell samples, the XPS C 1*s*, and Raman spectra of H-YS, Co_3O_4-H-YS, and $CoSe_2$-H-YS were analyzed, as shown in Figure 6c,d, respectively. The high-resolution XPS C 1*s* spectra of the three samples commonly exhibited three deconvoluted peaks around 284.5, 285.7, and 288.7 eV, which corresponded to C—C sp^3, C—O, and C—O bonds, respectively.[24,30] Owing to the surface oxidation as the cobalt-salt-infiltrated carbon yolk-shell was oxidized to form Co_3O_4-H-YS, in the C 1*s* spectrum of Co_3O_4-H-YS, the C—O and C—O peaks were relatively developed. In contrast, as $CoSe_2$-H-YS was formed in a reducing atmosphere, the C—O and C—O peaks were weakened compared with the carbon yolk-shell. The Raman spectra of the three samples in Figure 6d reflect the tendency of the results of the XPS C 1*s* spectra. The three samples exhibited separate D (1352 cm^{-1}) and G (1591 cm^{-1}) bands, attributed to defective carbon and graphitic carbon, respectively.[24,31] Moreover, to confirm the presence of N-doped carbon derived from PVP, the XPS N 1s spectrum of H-YS was analyzed, as shown in Figure S7, Supporting Information. The N 1s XPS spectrum reveals the presence of various N doping configurations such as pyridine N (399.4 eV), pyrrole N (400.7 eV), graphitie N (401.9 eV). According to the previous literature,[32,33] these N doping configurations cause the electronic state distortions, which are responsible for the improvement of electronic conductivity and chemical activity. This implies that the PVP-derived carbon can boost the electron/alkaline-ion transfer kinetics and provide better ion storage performance. The thermogravimetric (TG) curve of the Co_3O_4-H-YS in Figure S8, Supporting Information indicates that the carbon contents of Co_3O_4-H-YS are 28 wt%. The cobalt salt infiltrated carbon yolk-shell was also transformed into cobalt sulfide-carbon yolk-shell by a simple sulfidation process. As shown in Figure S9a, Supporting Information, the XRD patterns reveal the formation of Co_9S_8 phase, and the SEM images confirm complete infiltration of Co_9S_8 nanocrystals as well as the formation of yolk-shell after sulfidation process.

To demonstrate the synthesis potential of common metal compounds, we successfully synthesized other metal oxide–carbon yolk-shell samples, such as NiO and Fe_3O_4, by metal salt infiltration methods into highly porous carbon yolk-shell structures. The SEM images of NiO-H-YS and Fe_3O_4-H-YS show similar morphologies to that of Co_3O_4-H-YS, as shown in Figure S10a–d, Supporting Information. The SEM images of a broken microsphere reveal the formation of yolk-shell-structured microspheres even through metal salt infiltrations and oxidation. The XRD patterns in Figure S10e, Supporting Information confirm the formation of NiO and Fe_3O_4 phases in NiO-H-YS and Fe_3O_4-H-YS, respectively. In order to maintain the morphology of the shell stably even after posttreatment, we fabricated yolk-shell carbon microsphere with a thick shell by doubling the amount of PVP from the ratio of PVP/sucrose (1/4 wt%) (denoted as D-YS-TS). By improving the weight ratio of PVP, the thickness of the shell derived from PVP could be increased, and the spherical shape of the shell was improved accordingly as shown in Figure S11a, Supporting Information. Moreover, the spherical shape was well maintained even after the oxidation process, as shown in Figure S11b,c, Supporting Information. To verify the porosity increase of the carbon yolk-shell by adding magnesium component during the preparation of precursor powders in the spray pyrolysis process, carbon yolk-shell was prepared from a precursor, which was obtained by a spray solution with the same conditions except for magnesium salt; the morphological properties are shown in Figure S12, Supporting Information. The SEM images of the carbon yolk-shell structures with and without the assistance of magnesium salt were almost identical. However, the morphologies of Co_3O_4-H-YS and $CoSe_2$-H-YS, formed from the carbon yolk-shell without the assistance of magnesium salt (denoted as Co_3O_4-H-YS-WM and $CoSe_2$-H-YS-WM), exhibited cobalt compounds crystallized on the surface of the carbon shell. This indicates that in the case of carbon, where a sufficient porosity was not developed, the metal salt was not penetrated to the inside and was primarily impregnated outside, which promoted the crystal growth outward of the shell by the Ostwald ripening effect. To utilize the carbon yolk-shell as a reservoir for ultrafine nanocrystals, the effect of the addition of a magnesium component was very important.

To confirm the effectiveness of the cobalt compound–carbon yolk-shell structures as anode materials for alkali-ion batteries (lithium-, sodium-, potassium-ion batteries (LIBs, SIBs, and KIBs, respectively)), the electrochemical properties of the cobalt compounds (Co_3O_4, $CoSe_2$)–carbon yolk-shell structures as anode materials were investigated, as shown in **Figures 7–9**.

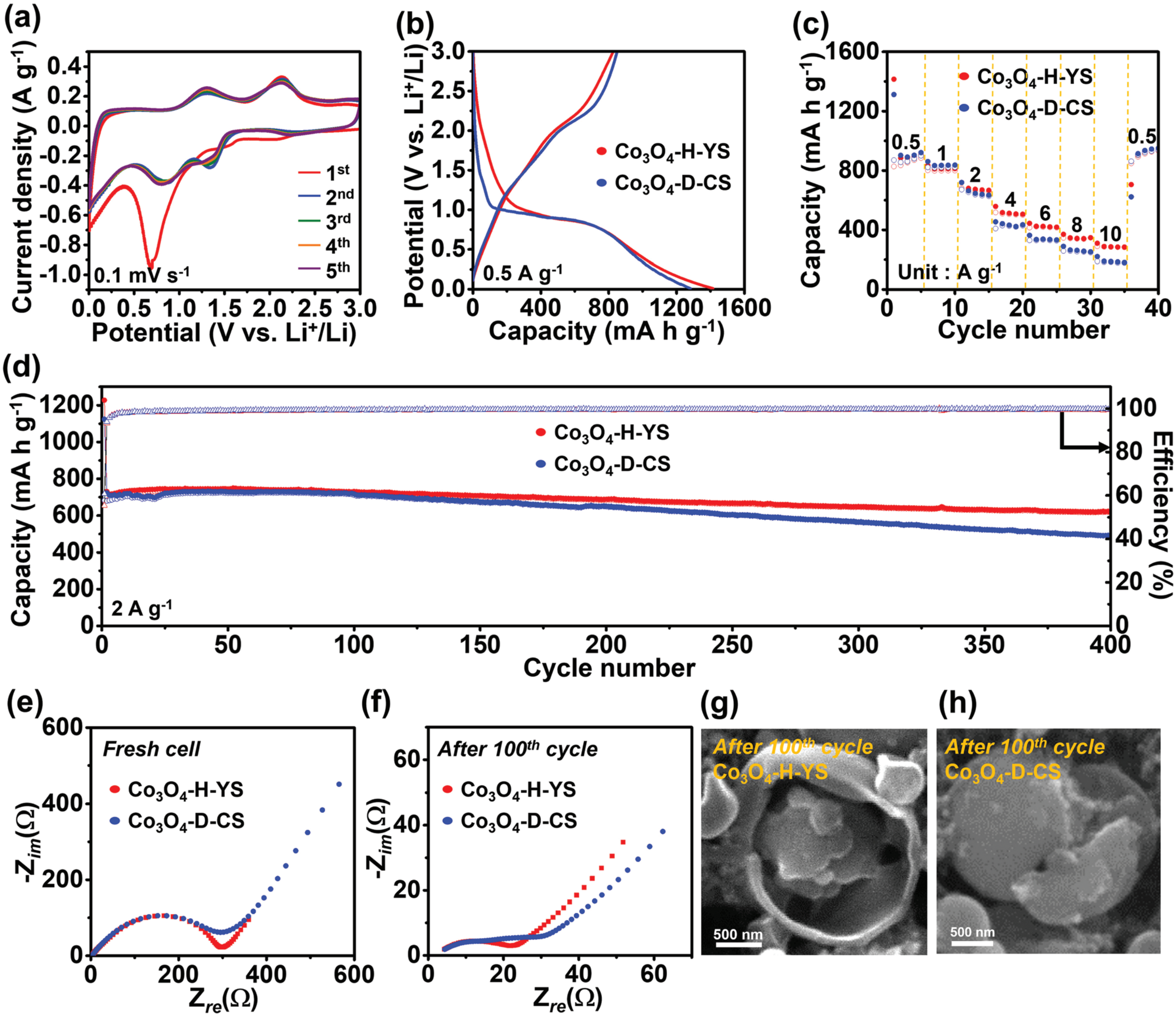

Figure 7. Electrochemical properties of Co_3O_4–H-YS, Co_3O_4-D-CS electrodes for LIBs. a) CV curves of Co_3O_4-H-YS, b) initial discharge and charge curves, c) rate performances, d) cycle performances at a current density of 2 A g^{-1}, e) Nyquist plots of fresh cells, f) Nyquist plots after 100 cycles, and SEM images after 100 cycles of g) Co_3O_4-H-YS and h) Co_3O_4-D-CS.

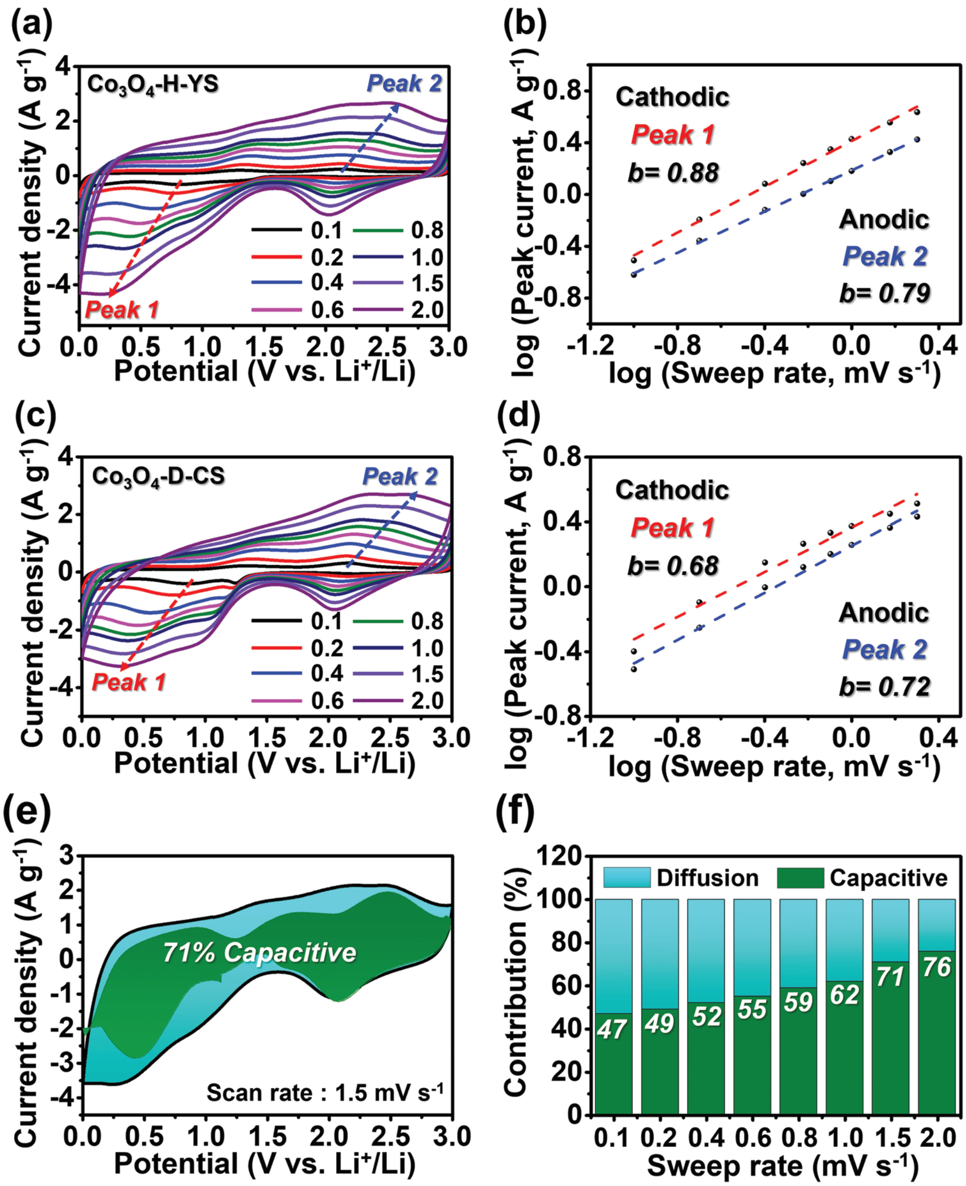

Figure 8. a) CV curves of Co_3O_4-H-YS at various sweep rates, b) fitted log (peak current) versus log (scan rate) for Peak 1 and Peak 2 of Co_3O_4-H-YS, c) CV curves of Co_3O_4-D-CS at various sweep rates, d) fitted log (peak current) versus log (scan rate) for Peak 1 and Peak 2 of Co_3O_4-D-CS, e) CV curves of Co_3O_4-H-YS showing capacitive contribution (green color shaded area) to the total current at a scan rate of 1.5 mV s^{-1}, and f) capacity contribution of Co_3O_4-H-YS at different scan rates.

The Co_3O_4-carbon yolk-shell was applied as an anode material for LIBs, whereas the $CoSe_2$-carbon yolk-shell was employed as an anode material for SIBs and KIBs. Cyclic voltammetry (CV) measurements on Co_3O_4-H-YS and Co_3O_4-D-CS were performed in a potential range of 0.001–3.0 V (vs Li$^+$/Li) at a scan rate of 0.1 mV s^{-1} for the initial five cycles, as shown in Figure 7a and Figure S13, Supporting Information, respectively. The CV curves of Co_3O_4-H-YS and Co_3O_4-D-CS exhibited analogous forms to those reported for Co_3O_4 electrode materials. In the initial cathodic sweep, an obvious peak at 0.73 V was observed; this was related to the conversion reaction from Co_3O_4 to metallic Co and Li_2O.[34,35] The two anodic peaks ≈1.3 and 2.1 V were attributed to the oxidation transformation from metallic Co/Li_2O to Co_3O_4 by two reversed steps.[34,35] After the second cycle, the reversible cathodic and anodic peaks corresponded to the reduction and oxidation of the metallic Co and Co_3O_4 phase, respectively. The initial discharge and charge potential profiles of Co_3O_4-H-YS and Co_3O_4-D-CS at a current density of 0.5 A g^{-1} are presented in Figure 7b. The two samples exhibited a plateau at 1 V approximately, corresponding to Li$^+$ insertion into the crystal structure of Co_3O_4 and reduction of the Co ions to metallic Co. Co_3O_4-H-YS and Co_3O_4-D-CS exhibited initial discharge capacities of 1415 and 1312 mA h g^{-1} and initial Coulombic efficiencies (ICE) of 58.4 and 66.2%, respectively. The lower ICE of Co_3O_4-H-YS than that of Co_3O_4-D-CS was owing to the more formation of a solid electrolyte interface (SEI) film

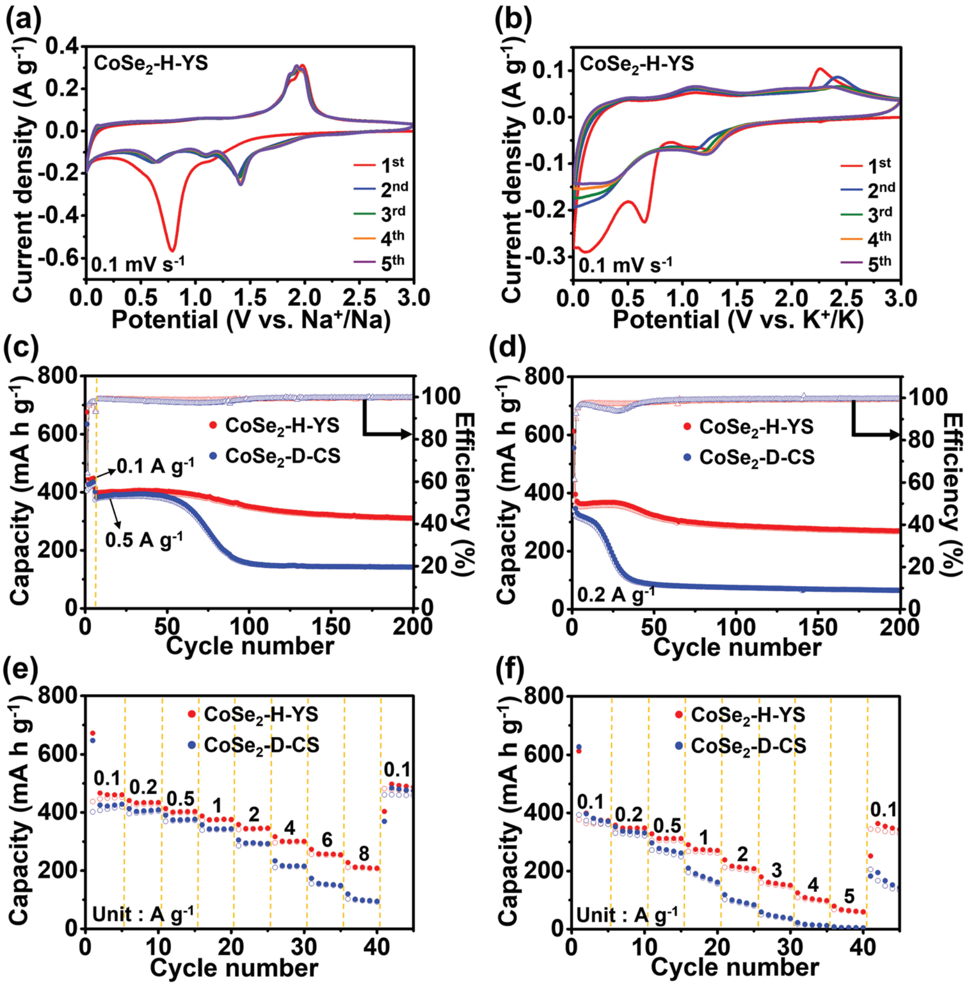

Figure 9. Electrochemical properties of $CoSe_2$-H-YS and $CoSe_2$-D-CS electrodes for a,c,e) SIBs and b,d,f) KIBs. CV curves of $CoSe_2$-H-YS at the scan rate of 0.1 mV s^{-1} for a) SIBs and b) KIBs. c) Cycle performances of $CoSe_2$-H-YS and $CoSe_2$-D-CS for SIBs at a current density of 0.5 A g^{-1} with activation first at a cycling rate of 0.1 A g^{-1} for five times. d) Cycle performances of $CoSe_2$-H-YS and $CoSe_2$-D-CS for KIBs at a current density of 0.2 A g^{-1}. Rate performances of $CoSe_2$-H-YS and $CoSe_2$-D-CS for e) SIBs and f) KIBs.

and organic polymeric gel-like layer by electrolyte decomposition during the first discharge process. The hollow nanocarbon aggregate@void@shell configuration with a porous structured shell provided good channels for the penetration of the electrolyte into the nanostructured active material, thereby uniformly forming a SEI film and contributing to the organic polymeric gel-like layer by electrolyte decomposition. The rate capabilities of Co_3O_4-H-YS and Co_3O_4-D-CS were compared, as shown in Figure 7c. Up to a relatively low current density of 2 A g^{-1}, the two samples exhibited similar rate properties; however, differences were observed at high current densities between 4 and 10 A g^{-1}. The porous and hollow structure of Co_3O_4-H-YS contributed to the small diffusion distance of the lithium ions, thereby resulting in an excellent rate capability. Moreover, the carbon substrate of the two samples provided stability even at a high current density of 10 A g^{-1}. The capacities of the two samples were stably recovered at a current density of 0.5 A g^{-1}. Co_3O_4-H-YS exhibited reversible discharge capacities of 905, 812, 667, 506, 420, 347, and 284 mA h g^{-1} at current densities of 0.5, 1, 2, 4, 6, 8, and 10 A g^{-1}, respectively. The capacity returned to 941 mA h g^{-1} when the current density was reduced to 0.5 A g^{-1}. The cycle performances of Co_3O_4-H-YS and Co_3O_4-D-CS at a current density of 2.0 A g^{-1} are shown in Figure 7d. During the initial 100 cycles, the two electrodes exhibited high cycle stabilities. After these cycles, Co_3O_4-D-CS exhibited a continuous capacity fading owing to structural destruction from the dense structure by volume change during the long-term cycling. However, Co_3O_4-H-YS maintained the high capacities over 400 cycles owing to the high structural stability. The discharge capacity of Co_3O_4-H-YS decreased slightly from 731 to 622 mA h g^{-1} from the 2nd cycle to the 400th cycle, whereas that of Co_3O_4-D-CS decreased rapidly from 723 to 491 mA h g^{-1} in the same cycle range. To get the actual lithium-ion storage of carbon component in the cobalt oxide and carbon composite, the cycle tests of bare hollow yolk-shell (H-YS) and dense core-shell (D-CS) anodes for LIBs were conducted as shown in Figure S14, Supporting Information. In this study, the carbon yolk-shell microspheres, which were derived from decomposition of PVP and sucrose under 1000 °C, had characteristic of amorphous and some of the hard carbon. Therefore, the initial

Coulombic efficiencies of H-YS and D-CS exhibited low values, which were ascribed to the formation of solid electrolyte interface (SEI) film and organic polymeric gel-like layer by electrolyte decomposition during the first discharge process into micropores inside or on the surface of a microsphere. After 400 cycles, the reversible discharge capacities of H-YS and D-CS are 261 and 119 mA h g^{-1} at a current density of 2.0 A g^{-1}, respectively. Considering carbon contents in the cobalt oxide–carbon composite, which was proved in the TG data (Figure S8, Supporting Information), the acutual capacity contributed by carbon in Co_3O_4-H-YS and Co_3O_4-D-CS after 400th cycle is calculated to 73 and 33 mA h g^{-1}. It revealed that hollow structured yolk carbon@void@shell configuration contributed to more reactive and storage sites for lithium ions compared to dense structured yolk@shell. To demonstrate the electrochemical superiority of Co_3O_4-H-YS, the cycle and rate performances of Co_3O_4-D-YS prepared by the spray solution with a ratio of PVP/sucrose 1/4 were analyzed, as shown in Figure S15, Supporting Information. Compared to Co_3O_4-D-CS, the yolk part exhibited a similar dense structure resulting in analogous electrochemical performances.

The lithium-ion storage performance of Co_3O_4-H-YS was superior to that of Co_3O_4-D-CS according to electrochemical impedance spectroscopy measurements before cycling and after 100 cycles, as shown in Figure 7e,f, respectively. The medium-frequency semicircle represents the charge transfer resistance (R_{ct}), whereas the line inclined at approximately 45° to the real axis represents the Li diffusion within the electrodes. Co_3O_4-H-YS and Co_3O_4-D-CS had similar R_{ct} values before the cycling, whereas a difference in R_{ct} was observed after 100 cycles. The additional semicircle observed for Co_3O_4-D-CS confirmed the formation of a thick SEI layer owing to the severe structural breaking during the repeated cycling. Co_3O_4-H-YS and Co_3O_4-D-CS had R_{ct} values of 21.8 and 36.5 Ω, respectively, after 100 cycles. These results were consistent with the difference between the structural morphologies after the cycling of the two samples, as shown in Figure 7g,h. The SEM images of Co_3O_4-H-YS and Co_3O_4-D-CS after 100 cycles indicate that the hollow nanosphere aggregated yolk@void@shell configuration structure had a structural stability compared with the dense structured microsphere during the repeated volume changes. The lithium-ion diffusion coefficient of Co_3O_4-H-YS and Co_3O_4-D-CS after 100 cycles was obtained by the straight line in the low-frequency domain of Nyquist plots in Figure 7e,f, respectively. The diffusion coefficient of Li-ions (D_{Li+}) can be calculated using the following equation

$$D_{Li+} = 0.5\left(RT/Sn^2F^2C\sigma\right)^2 \tag{1}$$

Information on the parameter values is available in the literature.[36] After 100 cycles, the relationship plot between the real part of the impedance (Z_{re}) and $w^{-1/2}$ after 100 cycles for Co_3O_4-H-YS and Co_3O_4-D-CS electrodes was shown in Figure S16, Supporting Information. Considering Warburg factor slope, the lithium-ion diffusion coefficients of Co_3O_4-H-YS and Co_3O_4-D-CS were calculated as 7.14×10^{-15} and 5.56×10^{-15} cm^2 s^{-1}, respectively. It revealed that hollow and porous structured yolk@void@shell configuration contributed to the enhanced lithium-ion diffusion properties.

CV rate tests were conducted at scan rates of 0.1, 0.2, 0.4, 0.6, 0.8, 1.0, 1.5, and 2.0 mV s^{-1} to compare the electrochemical kinetic properties of Co_3O_4-H-YS and Co_3O_4-D-CS, as shown in Figure 8. The CV curves of the two samples were commonly broadened and slightly shifted as the scan rate increased, which revealed the polarization of the electrodes. Through the CV curves at various scan rates, the relative diffusion and capacitive contributions of the samples were calculated using the equation:[37]

$$\log(i) = b\log(v) + \log(a) \tag{2}$$

where i is the measured current and v is the scan rate. A b-value close to 0.5 implies that the electrochemical behavior is controlled primarily by ionic diffusion, whereas a b-value close to 1.0 corresponds to a capacitive behavior dominating the total reaction. The b-values corresponding to the reduction and oxidation peaks in the two samples were obtained, as shown in Figure 8b,d. Co_3O_4-H-YS exhibited higher b values than those of Co_3O_4-D-CS at reduction (peak 1) and oxidation (peak 2). This implies that Co_3O_4-H-YS had a dominant surface-controlled behavior in the redox process owing to the porous and hollow structure compared with Co_3O_4-D-CS. Kinetic characterizations of the electrodes were performed by separating the capacitive capacity and diffusion-controlled capacity. The relative contributions at a fixed potential could be calculated using the equation:[38]

$$i(V) = k_1 v + k_2 v^{1/2} \tag{3}$$

where $k_1 v$ and $k_2 v^{1/2}$ correspond to the surface capacitive behavior and diffusion-controlled process, respectively. The capacitive contribution of the current at a specific potential can be determined by defining the values of k_1 and k_2. At a scan rate of 1.5 mV s^{-1}, the capacitive contribution (green color shaded area) of Co_3O_4-H-YS was 71%. This value continuously increased with the scan rate, reaching 76% at a high scan rate of 2.0 mV s^{-1} (Figure 8f). The ratio of the capacitive-controlled contribution of Co_3O_4-H-YS revealed a fast transport of the Li ions; this property improved the electrode rate capability.

The $CoSe_2$ yolk-shell microspheres ($CoSe_2$-H-YS and $CoSe_2$-D-CS) were applied as anode materials for SIBs and KIBs. Their electrochemical properties are shown in Figure 9. The CV curves of $CoSe_2$-H-YS and $CoSe_2$-D-CS in Figure 9a and Figure S17, Supporting Information exhibit typical cathodic and anodic shapes of cobalt diselenide as an anode for SIBs, as reported in the literature.[39–41] During the initial discharging process, several peaks at 1.15 and 0.79 V, related to the multistep electrochemical reactions, were observed, and attributed to Na-ion intercalation (Na_xCoSe_2) and conversion reactions (metallic Co and Na_2Se), respectively.[39–41] The distinct reduction peak at 0.79 V was also attributed to the decomposition of electrolyte and the formation of a SEI layer.[39,40] The considerable anodic peaks around 1.97 V could be attributed to the desodiation process.[40,41] The CV curves of $CoSe_2$-H-YS and $CoSe_2$-D-CS as anode materials for KIBs are presented in Figure 9b and Figure S18, Supporting Information. During the first cathodic sweep, the two electrodes exhibited distinct peaks at ≈1.1 and 0.65 V, corresponding to the K^+ ion insertion in the $CoSe_2$ crystal (K_xCoSe_2) and potassiation reaction from K_xCoSe_2 to Co and K_2Se as well as the formation of a SEI layer, respectively.[42,43]

The subsequent peak ≈0.01–0.1 V was related to the K^+ intercalation into the carbon yolk-shell matrix.[42,43] In the initial anodic sweep, the peaks at 1.08, 1.75, and 2.25 V were attributed to the stepwise transformation of potassium selenide and metallic Co into $CoSe_2$ nanocrystals, whereas the peak at 0.5 V corresponded to the release of K^+ from the carbon matrix.[42–45]

The galvanostatic discharge/charge curves of $CoSe_2$-H-YS and $CoSe_2$-D-CS in Figure S19, Supporting Information could be well-fitted to the redox peaks in the CV curves. The cycle performances of $CoSe_2$-H-YS and $CoSe_2$-D-CS as anodes for SIBs and KIBs are shown in Figure 9c,d, respectively. The initial increasing capacities of $CoSe_2$-H-YS for SIBs and KIBs are commonly attributed to partially structural destruction, and consequent formation of a polymeric gel-like film that was attributed to the reversible formation of SEI layers via the electrocatalytic effect of metallic Co nanocrystals.[46] Compared with the LIBs properties, the two electrodes exhibited differences regarding the cyclic stability. $CoSe_2$-D-CS for SIBs exhibited a stable cycle performance in the initial 50 cycles, whereas a large capacity decay was observed afterward. Moreover, $CoSe_2$-D-CS exhibited a rapid performance degradation for KIBs from the beginning. Thus, maintaining the stability of the electrode material in KIBs was more challenging compared with LIBs and SIBs.[47] In contrast, $CoSe_2$-H-YS exhibited excellent cyclic stabilities for both SIBs and KIBs. The structural merit of the hollow nanosphere aggregate@void@shell configuration contributed to the stable cycle performance even as an anode for KIBs. The discharge capacities of the $CoSe_2$-H-YS electrodes for SIBs and KIBs at the 200th cycle were 311 and 271 mA h g^{-1}, respectively, whereas those of the $CoSe_2$-D-CS electrodes for SIBs and KIBs were 142 and 100 mA h g^{-1}, respectively. Further, the $CoSe_2$-H-YS electrode exhibited excellent rate performances compared to $CoSe_2$-D-CS for SIBs and KIBs, as observed in Figure 9e,f, respectively. The porous and thin hollow shell consisting of $CoSe_2$-H-YS facilitated the shortened ion diffusion and fast electrolyte penetration compared to the dense structured $CoSe_2$-D-CS.[48] $CoSe_2$-H-YS for SIBs exhibited reversible discharge capacities of 461, 434, 404, 376, 346, 301, 255, and 209 mA h g^{-1} at current densities of 0.1, 0.2, 0.5, 1.0, 2.0, 4.0, 6.0, and 8.0 A g^{-1}, respectively, $CoSe_2$-H-YS for KIBs exhibited reversible discharge capacities of 373, 348, 312, 271, 208, 154, 98, and 60 mA h g^{-1} at current densities of 0.1, 0.2, 0.5, 1.0, 2.0, 3.0, 4.0, and 5.0 A g^{-1}, respectively. In contrast, $CoSe_2$-D-CS exhibited low reversible capacities of 95 and 5 mA h g^{-1} at high current densities of 8.0 and 5.0 A g^{-1} for SIBs and KIBs, respectively. To show the structural stability of $CoSe_2$-H-YS, the SEM images of $CoSe_2$-H-YS after 50 cycles as anode materials for SIBs and KIBs, respectively, were exhibited in Figure S20, Supporting Information. The yolk-shell configuration of $CoSe_2$-H-YS after cycling revealed their structural stability even though rapid volume expansion and contraction as anode materials of SIBs and KIBs.

Furthermore, $CoSe_2$-D-YS prepared by the spray solution with a ratio of PVP/sucrose 1/4 was produced to demonstrate the electrochemical superiority of $CoSe_2$-H-YS as anode materials for SIBs and KIBs. The SEM images in Figure S21, Supporting Information exhibited the formation of dense yolk@void@shell configuration structure of $CoSe_2$-D-YS. The electrochemical performances of $CoSe_2$-D-YS as anode materials for SIBs and KIBs are shown in Figure S22 and S23, Supporting Information. Interestingly, the cycling stabilities of $CoSe_2$-D-YS for SIBs and KIBs are obviously superior to those of $CoSe_2$-D-CS compared to properties of LIBs. Although the yolk was dense, it could be seen that it showed structural stability because of the space with voids in the process of Na or K-ion storages which had more severe rapid expansion and contraction than lithium-ions. However, regarding the rate characteristics, since there was no significant difference between $CoSe_2$-D-YS and $CoSe_2$-D-CS, it could be seen that the hollow and porous yolk structure of $CoSe_2$-H-YS has an effect to fast diffusion properties. It could be seen that the overall hollow and porous structure of the structure was an important factor for excellent properties in the alkali-ion storage property accompanied by volume expansion by the conversion reaction.

3. Conclusions

In this study, new synthesis strategies for nanostructured carbon yolk-shell microsphere that enable to control morphology and size of yolk part were first introduced. The specific characteristic of the carbon yolk-shell microsphere according to the ratio of PVP/sucrose in the spray solution was investigated. The prepared nanostructured carbon yolk-shell microsphere was utilized as an effective reservoir for ultrafine cobalt compound nanocrystals. Magnesium oxide was added to improve the pore volume capable of impregnating a metal salt. It was synthesized for the storage of metal compound nanocrystals. Cobalt compounds (cobalt oxide and cobalt selenide) were selected as the first target materials to form nanostructured cobalt compound–carbon composites as anode materials for alkali-ion batteries. This rational synthesis strategy could be employed to further improve their application potential in various fields, including energy storage and conversion, catalysis, fuel cells, and supercapacitors.

4. Experimental Section

The nanostructured carbon yolk-shell microsphere that enables to control morphology and size of yolk part were prepared by spray pyrolysis, selenization, and etching processes. The schematic diagram and digital photo of the spray pyrolysis system are shown in Figure S24, Supporting Information. During the spray pyrolysis process, droplets were generated using a 1.7-MHz ultrasonic spray generator consisting of six vibrators. The droplets were carried to a quartz reactor with a length of 1200 mm and diameter of 50 mm maintained at 400 °C using air as a carrier gas at a flow rate of 10 L min^{-1}. The spray solution was prepared by dissolving 0.2 M of Sn(II) oxalate, 0.05 M of magnesium nitrate hexahydrate, 8 g L^{-1} of PVP ($M_w = 40\,000$), and certain concentration of sucrose in 1 L of distilled water. In the case of mixing PVP and sucrose in the spray solution, the ratios of PVP/sucrose were 1/0, 1/1, 1/2, 1/4, and 1/8 wt%. The sprayed precursor powders were posttreated in a tube furnace at 1000 °C under a 10% H_2/Ar atmosphere for 3 h to produce MgSe-C@C microspheres. In the immediate SnSe-MgSe-C@C obtained by the selenization process, tin selenide component was completely evaporated under a high temperature of 1000 °C. The obtained MgSe-C@C microsphere was etched by an HCl/HNO_3 solution, thus resulting in the formation of a yolk-shell carbon microsphere. Based on 1 g of carbon yolk-shell microsphere powders, 3.5 g of cobalt nitrate hexahydrate ($Co(NO_3)_3 \cdot 6H_2O$, Samchun Chemical Co. Ltd.) was dissolved in a high-purity solution of ethyl alcohol. The solutions were infiltrated into carbon yolk-shell powders. Oxidation at 200 °C for 3 h under the air atmosphere transformed the cobalt nitrate-C yolk-shell into a Co_3O_4-C yolk-shell, whereas the selenization with a selenium powder at 300 °C under a 10% H_2/Ar atmosphere for 3 h transformed the cobalt nitrate-C yolk-shell into the $CoSe_2$-C yolk-shell. The NiO-C yolk-shell and Fe_3O_4-C yolk-shell microspheres were synthesized by the same under the air atmosphere. Detailed information pertaining to the characterization and electrochemical measurements of the prepared samples is provided in Supporting Information.

Supporting Information

Supporting Information is available from the Wiley Online Library or from the author.

Acknowledgements

This work was supported by a National Research Foundation of Korea (NRF) grant funded by the Korea government (MEST) (NRF-2022R1F1A1070886). This work was supported by Chungbuk National University BK21 program (2021). This research was supported by the grant of Korea Institute of Ceramic Engineering and Technology (KICET).

Conflict of Interest

The authors declare no conflict of interest.

Data Availability Statement

The data that support the findings of this study are available in the supplementary material of this article.

Keywords

alkali-ion batteries, carbon yolk-shell, nanostructure, porous carbon, reservoirs

Received: October 21, 2022
Revised: December 23, 2022
Published online:

---

[1] Y. Zhao, L. Jiang, *Adv. Mater.* **2009**, *21*, 3621.
[2] J. Liu, N. P. Wickramaratne, S. Z. Qiao, M. Jaroniec, *Nat. Mater.* **2015**, *14*, 763.
[3] G. Zhou, D.-W. Wang, X. Shan, N. Li, F. Li, H.-M. Cheng, *J. Mater. Chem.* **2012**, *22*, 11252.
[4] Z. L. Schaefer, M. L. Gross, M. A. Hickner, R. E. Schaak, *Angew. Chem., Int. Ed.* **2010**, *49*, 7045.
[5] B. Y. Xia, J. N. Wang, X. X. Wang, J. J. Niu, Z. M. Sheng, M. R. Hu, Q. C. Yu, *Adv. Funct. Mater.* **2008**, *18*, 1790.
[6] K. Xie, X. Qin, X. Wang, Y. Wang, H. Tao, Q. Wu, L. Yang, Z. Hu, *Adv. Mater.* **2012**, *24*, 347.
[7] R. Liu, S. M. Mahurin, C. Li, R. R. Unocic, J. C. Idrobo, H. Gao, S. J. Pennycook, S. Dai, *Angew. Chem., Int. Ed.* **2011**, *50*, 6799.
[8] X. Han, L. Sun, F. Wang, D. Sun, *J. Mater. Chem. A* **2018**, *6*, 18891.
[9] Y. Chen, S. Zhang, Y. Feng, G. Yang, H. Ji, X. Miao, *ChemElectroChem* **2020**, *7*, 5013.
[10] M. Wang, Y. Yang, Z. Yang, L. Gu, Q. Chen, Y. Yu, *Adv. Sci.* **2017**, *4*, 1600468.
[11] J. Wang, S. Feng, Y. Song, W. Li, W. Gao, A. A. Elzatahry, D. Aldhayan, Y. Xia, D. Zhao, *Catal. Today* **2015**, *243*, 199.
[12] H. Zhang, H. He, J. Luan, X. Huang, Y. Tang, H. Wang, *J. Mater. Chem. A* **2018**, *6*, 23318.
[13] J.-S. Park, S. Y. Yang, J.-K. Lee, Y. C. Kang, *J. Mater. Chem. A* **2022**, *10*, 17790.
[14] S. H. Yang, G. D. Park, J. K. Kim, Y. C. Kang, *Chem. Eng. J.* **2021**, *424*, 130341.
[15] S. H. Yang, S. K. Park, G. D. Park, J. H. Lee, Y. C. Kang, *Small* **2020**, *16*, 2002345.
[16] G. D. Park, J. H. Kim, Y. C. Kang, *Chem. Eng. J.* **2021**, *406*, 126840.
[17] Z. Zhu, S. Wang, J. Du, Q. Jin, T. Zhang, F. Cheng, J. Chen, *Nano Lett.* **2014**, *14*, 153.
[18] H. Hu, J. Zhang, B. Guan, X. W. Lou, *Angew. Chem., Int. Ed.* **2016**, *55*, 9514.
[19] S. Chen, X. Huang, B. Sun, J. Zhang, H. Liu, G. Wang, *J. Mater. Chem. A* **2014**, *2*, 16199.
[20] S. Wang, J. Teng, Y. Xie, Z.-W. Wei, Y. Fan, J.-J. Jiang, H.-P. Wang, H. Liu, D. Wang, C.-Y. Su, *J. Mater. Chem. A* **2019**, *7*, 4036.
[21] Y. J. Hong, J.-K. Lee, Y. C. Kang, *J. Mater. Chem. A* **2017**, *5*, 988.
[22] R. Guo, R. Wang, Z. Ni, X. Liu, *Appl. Phys. A* **2018**, *124*, 623.
[23] S. A. Pawar, D. S. Patil, J. C. Shin, *J. Ind. Eng. Chem.* **2017**, *54*, 162.
[24] G. D. Park, Y. C. Kang, *ACS Sustainable Chem. Eng.* **2020**, *8*, 17707.
[25] D. Kong, H. Wang, Z. Lu, Y. Cui, *J. Am. Chem. Soc.* **2014**, *136*, 4897.
[26] C. Alex, S. C. Sarma, S. C. Peter, N. S. John, *ACS Appl. Energy Mater.* **2020**, *3*, 5439.
[27] Z. Cai, Y. Bi, E. Hu, W. Liu, N. Dwarica, Y. Tian, X. Li, Y. Kuang, Y. Li, X. Q. Yang, *Adv. Energy Mater.* **2018**, *8*, 1701694.
[28] Y.-J. Huang, C.-P. Lee, H.-W. Pang, C.-T. Li, M.-S. Fan, R. Vittal, K.-C. Ho, *Mater. Today Energy* **2017**, *6*, 189.
[29] G. D. Park, J. H. Hong, J. H. Choi, J. H. Lee, Y. S. Kim, Y. C. Kang, *Small* **2019**, *15*, 1901320.
[30] G. D. Park, J. S. Cho, Y. C. Kang, *Nano Energy* **2015**, *17*, 17.
[31] Y. Luan, R. Hu, Y. Fang, K. Zhu, K. Cheng, J. Yan, K. Ye, G. Wang, D. Cao, *Nano-Micro Lett.* **2019**, *11*, 30.
[32] Y. Li, M. Chen, B. Liu, Y. Zhang, X. Liang, X. Xia, *Adv. Energy Mater.* **2020**, *10*, 2000927.
[33] J. Ren, Y. Huang, H. Zhu, B. Zhang, H. Zhu, S. Shen, G. Tan, F. Wu, H. He, S. Lan, *Carbon Energy* **2020**, *2*, 176.
[34] M. Chen, X. Xia, J. Yin, Q. Chen, *Electrochim. Acta* **2015**, *160*, 15.
[35] W. Xu, X. Cui, Z. Xie, G. Dietrich, Y. Wang, *Electrochim. Acta* **2016**, *222*, 1021.
[36] Z. Wang, K. Dong, D. Wang, S. Luo, X. Liu, Y. Liu, Q. Wang, Y. Zhang, A. Hao, C. He, *Chem. Eng. J.* **2020**, *384*, 123327.
[37] Z. Yi, Y. Qian, J. Tian, K. Shen, N. Lin, Y. Qian, *J. Mater. Chem. A* **2019**, *7*, 12283.
[38] Y. Yoo, G. D. Park, Y. C. Kang, *Chem. Eng. J.* **2019**, *365*, 193.
[39] X. Hu, X. Liu, K. Chen, G. Wang, H. Wang, *J. Mater. Chem. A* **2019**, *7*, 11016.
[40] J. Yang, H. Gao, S. Men, Z. Shi, Z. Lin, X. Kang, S. Chen, *Adv. Sci.* **2018**, *5*, 1800763.
[41] J. S. Cho, J. M. Won, J.-K. Lee, Y. C. Kang, *Nano Energy* **2016**, *26*, 466.
[42] S. H. Yang, S.-K. Park, Y. C. Kang, *Nano-Micro Lett.* **2021**, *13*, 9.
[43] Z. Zhao, C. Gao, J. Fan, P. Shi, Q. Xu, Y. Min, *ACS Omega* **2021**, *6*, 17113.
[44] Z. Zhang, B. Zhang, J. Xu, M. Zhang, L. Duan, J. Shen, X. Zhou, *ACS Appl. Energy Mater.* **2021**, *4*, 6356.
[45] X. Sun, S. Zeng, R. Man, L. Wang, B. Zhang, F. Tian, Y. Qian, L. Xu, *Nanoscale* **2021**, *13*, 10385.
[46] J. Bai, X. Li, G. Liu, Y. Qian, S. Xiong, *Adv. Funct. Mater.* **2014**, *24*, 3012.
[47] J. Zhang, L. Lai, H. Wang, M. Chen, Z. Shen, *Mater. Today Energy* **2021**, *21*, 100747.
[48] J. Zhang, Y. Li, X. Liang, Q. Liu, Q. Chen, M. Chen, *Small* **2022**, *18*, 2106074.